JAAS

ROYAL SOCIETY OF CHEMISTRY

PAPER

View Article Online
View Journal | View Issue

Cite this: J. Anal. At. Spectrom., 2025, 40, 2126

In situ measurement of sulfur isotope ratios in sulfide samples with LA-ICP-MS/MS using N_2O and He reaction gas†

Estida Eensoo, *[a] Päärn Paiste,[a] Kärt Paiste,[ab] David A. Fike[b] and Jennifer L. Houghton[b]

Sulfur isotope signatures ($\delta^{34}S$) in sulfide minerals such as pyrite and pyrrhotite may reflect the specific geological conditions at their genesis. Understanding the $\delta^{34}S$ variability can help track (bio)–geochemical processes, from ore formation to finding evidence of early life. However, as sulfide mineral growth can occur at various stages of rock history, traditional bulk S isotope analysis can incorporate mixed geochemical signals generated by unrelated processes. *In situ* analytical techniques can be used to investigate compositional changes in $\delta^{34}S$ caused by early environmental or secondary processes. In this study, we aim to characterize $\delta^{34}S$ variability in pyrite and pyrrhotite using laser ablation inductively coupled plasma tandem mass spectrometry (LA-ICP-MS/MS) while introducing a mixture of N_2O and He in the reaction chamber to remove polyatomic interferences at $m/z = 32$ and $m/z = 34$. Alongside tuning the respective laser and ICP parameters, we employ a self-developed signal-smoothing device consisting of coiled thermoplastic elastomer (TPE) tubing and a cyclonic spray chamber to achieve better signal stability. In this way, we propose a new, fast, *in situ* screening approach for measuring the $\delta^{34}S$ of sulfides.

Received 28th April 2025
Accepted 19th June 2025

DOI: 10.1039/d5ja00166h

rsc.li/jaas

1. Introduction

Pyrite (FeS_2) and pyrrhotite (FeS), as part of the sulfide minerals category, are widely found in various geological environments, and they serve as valuable indicators in exploring geochemical processes. The genesis of pyrite occurs under a diverse set of conditions, from sediment deposition to multiple stages of metamorphism, resulting in petrographically distinct pyrites with diagnostic sulfur isotope and trace element compositions. Pyrrhotite may also appear in early or late stages of rock formation; however, it is metastable in low-temperature sedimentary environments where it converts to pyrite.[1] These iron sulfides exhibit $\delta^{34}S$ compositions that reflect the changes in the chemistry of mineralizing fluids and allow differentiation between biogenic and abiogenic sulfur cycling processes.[2] Therefore, the sulfur isotopes in pyrite and pyrrhotite are powerful tools for investigating processes such as sulfide-gold-ore formation,[3–5] tracking oil generation and migration in petroleum reservoirs,[6,7] as well as for searching for evidence of early life in Earth and beyond,[2,8] and biogeochemical processes throughout Earth's history.[9]

Regardless of the specific formation pathway, the genesis of FeS_2 and FeS typically occurs in diffusively limited environments where the mineralizing fluid's properties affect mineral crystallization and chemical composition. Since the expression of S isotope fractionations is sensitive to open-vs-closed system conditions, heterogeneous $\delta^{34}S$ signatures can form on the micro-scale and be preserved in iron sulfides that precipitate over time in evolving environmental conditions.[9–11] In addition, late-stage processes can introduce secondary sulfur- and metal-bearing fluids into sedimentary systems, thereby inducing the precipitation of multiple generations of genetically and isotopically distinct sulfide species.[9,12–14] In addition, as the temperature rises during metamorphism, pyrite can transform into pyrrhotite, and this process can reverse during the cooling stages of metamorphism.[15] On a bulk scale, isotopic fractionations accompanying the conversion of pyrite to pyrrhotite or *vice versa* are small;[16,17] however, isotopic zoning within individual crystals can develop.[15,18] Consequently, specific environmental conditions and late-stage alteration can lead to significant pyrite and pyrrhotite compositional variability, undetectable by traditional bulk extraction methods. During the commonly applied chromium-reducible sulfur (CRS) and acid-volatile sulfur (AVS) extractions,[19] the sulfur isotope variability is homogenized as the different components of a sample are combined. In contrast, petrographic investigations

[a]Department of Geology, University of Tartu, Tartu, 50411, Estonia. E-mail: estida@ut.ee; estida.eensoo@gmail.com

[b]Department of Earth, Environmental & Planetary Sciences, Washington University in St Louis, St Louis, MO, 63130, USA

† Electronic supplementary information (ESI) available. See DOI: https://doi.org/10.1039/d5ja00166h

combined with high-resolution sulfur isotope analysis allow for a more comprehensive approach to assessing the processes and factors influencing mineral growth, recrystallization, and alteration.

The traditional CRS and AVS extraction techniques are complemented by high-resolution techniques capable of $\delta^{34}S$ measurements, such as secondary ion mass spectrometry (SIMS) and laser ablation inductively coupled mass spectrometer (LA-ICP-MS), allowing for finer detailed analysis with minimal sample preparation.[20] Even though SIMS offers superior spatial resolution and high precision and accuracy in measuring sulfur isotope ratios,[21–23] it is less accessible, more complex to operate, and unsuitable for large sample quantities.[24] Alternatively, rapid developments in the field of LA-ICP-MS[25–27] have made it a viable, time- and cost-efficient alternative for *in situ* sulfide $\delta^{34}S$ measurements. Especially the introduction of multiple collector ICP-MS (MC-ICP-MS) has enabled high precision and rapid isotope ratio measurements, and thus, significant effort has been placed into improving such instruments' application in geological research.[26,28,29] On the other hand, tandem ICP-MS/MS, although favoured for its affordability, versatility, speed, and efficiency in routine elemental analyses, has received relatively little attention in stable isotope measurements due to its comparatively lower precision. In sulfur isotope analysis, the presence of isobaric effects at mass-to-charge ratios $m/z = 32$ and $m/z = 34$, mainly from O_2 and at $m/z = 32$ from NO have limited the application of tandem systems. Despite this drawback, the possibility of using so interferences at the masses of interest shows promise in expanding the LA-ICP-MS/MS application in determining $\delta^{34}S$ of iron sulfide minerals.[27] Here, we build upon the idea to improve the application of LA-ICP-MS/MS as a fast-screening method for pyrite and pyrrhotite $\delta^{34}S$ measurements in geosciences.

2. Experimental

2.1 Samples and in-house reference materials

We selected five sulfide samples with unknown $\delta^{34}S$ compositions. A vein pyrite collected from the Maksovo open-pit quarry near the village of Shunga, where the rocks from the Paleoproterozoic Zaonega formation are exposed (Onega Basin, Karelia, Russia; coordinates 62°35′35″N, 34°56′52″E). The Zaonega formation's coarse (mm-sized individual crystals) anhedral pyrite from a laminated quartz vein shows vein selvage overgrowth texture, suggesting it grew relatively late in vein development. Additionally, the study involved four Paleoproterozoic graphitic schist samples containing pyrrhotite from the Uljaste küla drill core (Ida-Viru County, Estonia, coordinates 59° 21′25.19″N 26°47′. 7.79″E), at depths of 227.8 m, 249.9 m, 305.1 m, 317 m, and 334.5 m. The unknown pyrite sample in this article is referred to as Zf-pyrite, and the pyrrhotite samples are called Uljaste pyrrhotites.

During the experiments, we applied an in-house pyrite reference material provided by D. Fike (Washington University in St Louis) and obtained from Ward's Science (Rochester, NY, USA). Previously conducted isotopic ratio mass spectrometry (IRMS) analysis assigned Ward's pyrite a $\delta^{34}S$ value of $-1.0 \pm 0.2‰$ (V-CDT).[22] SIMS analysis has shown a fragment-to-fragment reproducibility of $\pm 1.9‰$ and intra-fragment reproducibility of $\pm 2.8‰$ for Ward's pyrite.[22] We utilized a mm-sized porphyroblast Balmat pyrite obtained from J. Valley (University of Wisconsin–Madison) as a quality control pyrite sample between pyrite's analytical runs. The Balmat sample is well characterized and previously proposed as a potential S isotope reference material.[20] The Balmat sample has an IRMS $\delta^{34}S = 15.1 \pm 0.2‰$ (V-CDT), intra-crystal reproducibility within 0.1‰20, and inter-crystal variability $\delta^{34}S$ in the range of 14.4–14.9‰.[26] However, $\delta^{34}S$ values from 13.8 to 16.4‰ have also been reported for this pyrite.[20,26,30–32] During the tuning procedures for the ICP-MS/MS instrument, an approximately four cm-sized cubic hydrothermal pyrite crystal from the Huanzala mine (Huánuco, Peru coordinates 9°55′04″S 76°59′50″W) was used. A pyrrhotite obtained from Ward's Science and provided by D. Fike, was also used as in-house reference material with a preliminary working value of $\delta^{34}S = -0.11 \pm 0.5$ (V-CDT) ‰ determined by IRMS analysis.

The Zf-pyrite and the Huanzala pyrite rock specimens, which subsequently cut into smaller approximately 1 cm^3 sections to allow mounting into the ablation cell. The samples underwent a systematic grinding and polishing process to prepare an even and well-polished surface for analysis. Initially, the samples were ground using silicon carbide grinding papers from Buehler Metallography with index $P = 2500$ and $P = 4000$, followed by a series of diamond polishes using 9 μm, 6 μm, 3 μm, and 1 μm solutions. Afterward, we cleaned the samples with ethanol to remove any possible residues. The individual grains of Ward's pyrrhotite and Balmat's pyrite were embedded in a round (d = 25 mm) epoxy mount. The Ward's pyrite sample was an irregularly shaped rock (~1 cm in diameter); therefore, to prepare it for LA-ICP-MS/MS analysis, it was also embedded in epoxy. The sample mounts were ground and polished, following the same steps as the Zf and Huanzala pyrite. In addition, the Estonian Geological Survey provided the Uljaste pyrrhotite samples, which were polished thick sections.

2.2 IRMS analysis

We determined the $^{34}S/^{32}S$ ratios in pyrite and pyrrhotite samples from powdered specimens obtained through micro-drilling (Minimo One Series Ver.2 micro grinder, with 1 mm diamond-coated drill bit) at adjacent locations. Specifically, we drilled a grid of 16 spots (4 × 4) equally spaced from each other on the crosscut 4 × 4 cm Huanzala pyrite sample, covering the sample surface (Fig. S1, in ESI†). Additionally, five replicates were drilled on the surface of Ward's pyrite, and two replicates were sampled on Zf-pyrite (including one from the vein and one from non-vein Zf-pyrite). Similarly, for each of the Uljaste pyrrhotite samples, we extracted two adjacent replicates from the pyrrhotite veins. The limited number of pyrrhotite replicates was due to the small areas of pyrrhotite in the Uljaste samples. Prior characterization of the Uljaste samples was conducted using reflective light microscopy and a ZEISS EVO MA15 scanning electron microscope (SEM) at the Department of Geology,

University of Tartu. The SEM images were used to identify optimal drilling locations.

Around 300 μg of the drilled powdered material was loaded into tin capsules with excess V_2O_5. We measured the $^{34}S/^{32}S$ ratios using a Thermo Flash HT Element Analyzer connected with Thermo Delta B plus IRMS *via* ConFlo IV open split device at the University of Tartu. The sulfur isotope compositions are expressed in standard delta notation as per mil ($\delta^{34}S$ in ‰) deviations from the Vienna Canyon Diablo Troilite (V-CDT) standard[33] as follows:

$$\delta^{34}S_{VCDT}\ (‰) = [(^{34}S/^{32}S)_{sample}/(^{34}S/^{32}S)_{VCDT} - 1] \times 1000 \quad (1)$$

To calibrate the S isotopic ratios (IR) values, international standards composed of $BaSO_4$ such NBS-127 and IAEA-SO-6 were included in each analytical run. Four aliquots of each international standard were analysed-two at the beginning and two at the end of each analytical run to assess the instrumental stability over time. The $\delta^{34}S$ value of NBS-127 is 20.3 ± 0.2‰, while the operating value of the IAEA-SO-6 reference material is -34.1 ± 0.2‰.

2.3 LA-ICP-MS/MS analysis

We performed the sulfur isotope measurements at the University of Tartu utilizing a Cetac LSX-213 G2+ laser system with a HelEx II fast-washout two-volume large format cell using 800 mL per min helium as carrier gas. The LSX-213 G2+ system features an Nd: YAG laser (Neodymium-Doped Yttrium Aluminium Garnet). Typically, we ablated the samples at locations adjacent to the micro-drilled craters created by IRMS (see Fig. 1 below).

The pyrite and pyrrhotite samples and standards are ablated in the same analytical run and placed evenly in the sample holder (12 cm × 12 cm × 1 cm). Subsequently, the composition of the ablated material was analysed using an Agilent 8800 quadrupole ICP-MS/MS.

2.3.1 Signal smoothing experiments. Formerly, Gilbert *et al.* (2014)[26] showed that the addition of signal smoothing components, *e.g.*, "squid," a coiled tubing, and a glass bulb, between the laser and the ICP-MS, produces a more stable signal and improves measurement uncertainty and reproducibility. Thus, this experiment implemented four distinct

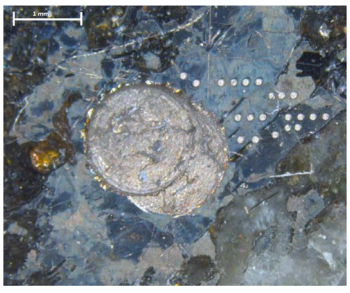

Fig. 1 Microscopic images of the Uljaste 304.5 pyrrhotite sample showing the micro-drilled crater's location and the LA-ICP-MS/MS spots. IRMS spot $d = 1$ mm, LA-ICP-MS spot $d = 100$ μm.

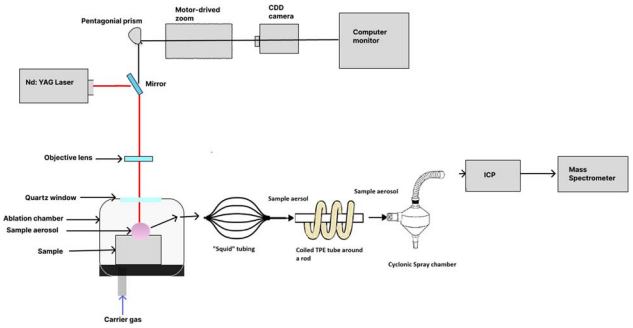

Fig. 2 Signal smoothing configuration D connecting to "squid" compartment, composed of 5 times coiled TPE tubing around a cylinder (O.D. 7 mm) and a cyclonic spray chamber, which connects to the ICP-MS system.

interface-tubing configurations to investigate signal stability and washout times on S reaction product signals (SO^+ and SO_2^+) signals using N_2O as the reaction gas. Each configuration featured a "squid" mixing device as a common component that distributes the sample aerosol between ten tubing before recombining and delivering it to the ICP. The four configurations are listed below:

Configuration A: this setup included a straight 20 cm polypropylene-based thermoplastic elastomer (TPE tube from Pharmed® BPT) with an internal diameter of 1.52 mm connected to the "squid" device and the ICP.

Configuration B: this setup consisted of the same TPE tubing coiled 5 times around a cylinder with a 7 mm outer diameter (O.D) attached to the "squid" device.

Configuration C: the same TPE tubing without coiling was connected to the "squid" device paired with a cyclonic spray chamber (Agilent Isomist Spray Chamber).

Configuration D: the configuration combined the TPE tubing coiled 5 times around a cylinder with 7 mm O.D., with the "squid" and the cyclonic spray chamber (see Fig. 2).

During these experiments, the sulfur signal was measured as two primary reaction products: SO^+ and SO_2^+. Sulfur ions were detected at specific mass-to-charge (m/z) ratios: $m/z = 48$ for $^{32}S^{16}O^+$ and $m/z = 50$ for $^{34}S^{16}O^+$ in case of SO^+, and $m/z = 64$ for $^{32}S^{16}O_2^+$ and $m/z = 66$ for $^{34}S^{16}O_2^+$ in case of SO_2^+.

The laser parameters for measuring sulfur signals as SO^+ reaction products included the spot size set at 40 μm, fluence at 10 J cm^{-2}, and repetition rate of 10 Hz. For measuring sulfur signals as SO_2^+ reaction product, configurations included a 50 μm spot size and fluence of 19.5 J cm^{-2}, while maintaining the repetition rate at the same value. Each ablation ran for 90 seconds: 20 s for warming up the laser, followed by the next 40 s for ablation, and 30 seconds for cooling down the laser. On the ICP-MS/MS, the sampling depth was changed between SO and SO_2-based experiments, corresponding to 6.0 mm for measuring SO^+ and 7.0 mm for SO_2^+ reaction products. We tuned the ICP-MS/MS to maintain the $^{32}S^{16}O^+$ and $^{32}S^{16}O_2^+$ signal counts of reaction product below 10^6 counts per second (cps), while dwell times were at 0.0465 s for each product ion mass. During this experiment, the 4th cell gas's operating flow was at 40%. The ablation targeted nine evenly spaced spots on

the surface of the Huanzala pyrite (100 μm apart) for each configuration. To characterize the outcomes of this experiment, we use the reproducibility of the non-drift corrected S isotope ratios, measurement uncertainty, and washout time.

2.3.1.1 Reproducibility of the non-drift corrected sulfur isotope ratios. Background-corrected S signals from nine ablations for each signal-smoothing configuration provided the data needed to calculate reproducibility. Data extraction was done through Iolite 3.62 software, where we defined sections for individual baselines and sample signals. Additionally, we used the "Mean without Outlier Rejection" option to allow the software to generate sulfur isotope ratios. The reproducibility is presented as the relative standard deviation in ‰ without applying additional drift correction (eqn (2)).

$$\mathrm{RSD}(‰) = \frac{\sqrt{\sum_{i=1}^{n}(x_i - \bar{x})^2}}{\frac{\sum_{i=1}^{n} x_i}{n}} \times 1000 \quad (2)$$

where x_i: sulfur isotope ratios from individual spots. $\bar{x}$: mean value of sulfur isotope ratios. n: number of measurements ($n = 9$).

2.3.1.2 Measurement uncertainty. We calculated the measurement uncertainty to assess the stability of the non-drift corrected sulfur isotope ratios during the ablation of the nine spots for each signal-smoothing configuration. For each spot, we then calculated the standard deviation of these uncorrected isotope ratios, expressed in ‰. The overall measurement uncertainty for each configuration was calculated by taking the mean standard deviation of the nine spots (eqn (3)).

$$\text{Mean standard deviation}(‰) = \frac{\sum_{i=1}^{n} s_i}{n} \times 1000 \quad (3)$$

where s_i: individual standard deviations of sulfur isotope measurements for each ablation. n: number of measurements ($n = 9$).

2.3.1.3 Washout. Our primary goal was to obtain a smooth ablation profile by keeping the time between analyses (*e.g.*, washout) as short as possible. By washout, we refer to the time it takes for the signal to decrease to the initial background level at the end of ablation. To calculate the washout, we take the ratio of the average counts per second (cps) between two distinct time intervals (A) 3 seconds before turning off the laser, and (B) 8–10 seconds after turning off the laser or, alternatively, between A and (C) 18–20 seconds after turning off the laser. Washout is especially troublesome for ablating sulfides due to the slow desorption of sulfur species from the inlet line.[25,34] The so-called memory effects associated with S species cause longer delays between analyses and increase the fraction of time spent on data acquisition.

2.3.2 Reaction gas experiments. This study compares the effectiveness of N_2O[27] and a mixture of N_2O with He as reaction/collision gases to reduce polyatomic interferences from O_2^+ and NO^+ ions at $m/z = 32$ and $m/z = 34$. The reactions between sulfur and nitrous oxide produce SO^+ ($m/z = 48$ for ^{32}S and $m/z = 50$ for ^{34}S) and SO_2^+ ($m/z = 64$ for ^{32}S and $m/z = 66$ for ^{34}S) ions as the main reaction products. While using N_2O and the N_2O–He combination, we monitored the SO^+ and SO_2^+ signal intensities in pulse mode through line scans ablated on Huanzala pyrite. The laser parameters included a 40 μm spot size, 8 J cm^{-2} fluence, 10 Hz repetition rate, and a 10 μm s^{-1} scan speed.

In the first set of experiments, we investigated the reaction product distribution for pure N_2O, increasing the gas flow rate from 10% to 100% in 5% increments. In the second set, we fixed the N_2O flow rates at 5%, 10%, 15%, and 20% while progressively adding He from 1 to 7 mL min^{-1} during a continuous ten-minute line scan. All ICP-MS/MS tuning parameters remained consistent between the two experiments, except for the energy discrimination. For the N_2O experiment alone, the energy discrimination value was set at −3 V, and for the N_2O–He experiment at −7 V, to achieve the highest signal output for the main reaction products. Following each change in N_2O or He gas flow rate, we allowed the signal to stabilize for 30 seconds. The reported signals in this experiment result from recording a 20 seconds online signal measurement and calculating its average.

2.3.3 Effect of detection mode and sample matrix on $\delta^{34}S$ measurements. During this part of the investigation, we aimed to characterize the application of Ward's pyrite and pyrrhotite as reference materials for measuring $\delta^{34}S$ in pyrite and pyrrhotite using the LA-ICP-MS/MS. A key focus of our tests was to analyze the behavior of the $^{32}S^{16}O$ and $^{34}S^{16}O_2$ signals in analog and pulse modes of the electron multiplier detector. For this reason, the instrument is tuned to maintain the sensitivity in three distinct counting range combinations on the detector:

Combination 1: both S reaction product signals are maintained in pulse mode for spot analysis.

Combination 2: $^{34}S^{16}O_2$ in pulse mode, while $^{32}S^{16}O$ in analog mode for line scans.

Combination 3: $^{34}S^{16}O_2$ in pulse mode, while $^{32}S^{16}O$ in analog mode for spot analysis.

During these experiments, both monitored masses had dwell times of 0.05 s with a total sampling period of 0.114 s.

Table 1 Operational parameters of the laser ablation system during the detection modes experiments[a]

Sample type	Analysis mode	Spot size (μm)	Fluence (J cm^{-2})	Repetition rate (Hz)	Scan speed (μm s^{-1})
Pyrite samples	Spot	50	10	5	—
	Lines	40	8	10	10
Pyrrhotite samples	Spot	100	10	5	—
	Lines	100	8	8	10

[a] Laser firing time consisted of 20 s of gas background, 40 s of ablation, and 30 s wash out.

Parameters that were tuned the same during the analysis in different detection modes were reflected power (1100 V), sampling depth (5 mm), and wait time offset (5 s). Additional ICP-MS/MS tuning parameters that differed during our analytical modes were He flow rate (2.5 mL min^{-1} in pulse–pulse, 4.5 mL min^{-1} in pulse-analog), 4th gas flow (15% in pulse–pulse and 5% in pulse-analog), and energy discrimination (−3 V in pulse–pulse and −7 V in pulse-analog). For pulse–pulse mode experiments, the $^{32}S^{16}O$ signal intensity was in the range of 8–9 × 10^5 cps for all samples, while for pulse-analog mode experiments, the $^{34}S^{16}O_2$ signal was tuned to the same range. We adjusted the laser parameters for each pyrite and pyrrhotite sample to achieve a smooth ablation signal profile. Pyrite and pyrrhotite samples usually display similar ablation characteristics within the respective group (see Table 1). During the ablation of Ward's pyrrhotite, hidden cracks became visible on the sample surface. To mitigate their impact, pre-ablation was conducted to expose and exclude these areas from subsequent ablations.

The normalization of the $\delta^{34}S$ is done by following the sample-standard-bracketing approach (SSB) applying both Ward's pyrite and Ward's pyrrhotite.[35] Before the $^{34}S/^{32}S$ measurements, we conditioned the plasma by ablating 50 spots randomly allocated on the Huanzala pyrite. After stabilizing the plasma, the sequence began with the ablation of five spots on Ward's pyrite standard, followed by five spots on the Zf-pyrite, five spots on the pyrrhotite standard, and lastly, five spots on the Uljaste pyrrhotite. This cycle of ablating 5 spots of the standards before samples was repeated four times.

2.3.4 S isotope ratio measurements on natural pyrite and pyrrhotite samples. The ablation of pyrite samples was performed using a spot size of 50 μm, fluence 10 J cm^{-2}, and a repetition rate of 5 Hz. The pyrrhotite group of samples was ablated using 100 μm spots, a fluence of 10 J cm^{-2}, and a varied repetition rate of 5–7 Hz among samples. Referring to the results of the signal smoothing and reaction gas optimization experiments (see Results and discussions), we opted to use the "squid" device, a seven-times coiled TPE tubing, and the cyclonic spray chamber for the smoothest ablation profile and N_2O–He mixture to amplify the SO^+ product ion signal. The SO^+ signal was measured at $m/z = 48$ and $m/z = 50$ for $^{32}S^{16}O^+$ and $^{34}S^{16}O^+$, respectively. The dwell times were 0.05 s for each mass, with a total sampling period of 0.114 s. During measurements, the $^{32}S^{16}O^+$ signal was kept under 10^6 cps. Additional operational parameters for ICP-MS/MS during this analysis are presented in Table 2.

Table 2 Operational parameters of the ICP-MS/MS compartment while measuring the natural samples

Parameter (unit)	Assigned value
Forward power (V)	1170
Nebulizer gas flow (mL min^{-1})	1.10
Extract lenses 1 & 2 (V)	−24.0 & −210.0
He flow rate (mL min^{-1})	4.5
4th reaction gas flow rate (%)	5
Sampling depth (mm)	5.0
Energy discrimination (V)	−7
Wait time offset (ms)	5

Initial data reduction of LA-ICP-MS/MS data for all experiments was performed using Iolite 3.62 software. Each ablation signal was manually integrated whereby the most stable ablation region was selected, excluding regions with signal spikes. Additionally, the sample backgrounds were manually defined to exclude any spikes. Furthermore, every crater was visually investigated after ablation, and signals from craters that revealed cracked surfaces or mixed ablation of sulfides and surrounding matrix were excluded further data processing (Fig. S4, in ESI†). Afterwards, the software algorithm calculates the raw isotopic ratio for each spot. We have selected the "mean with no outlier rejection" option so the software calculates the average using all data points. The generated signals were exported for post processing in Microsoft Excel. For $\delta^{34}S$ calculations, a second or third order polynomial fit was used for mass bias correction by using the signals of Ward's pyrite and pyrrhotite as in-house reference materials. The polynomial curve was applied to account for the instrumental mass bias, where we applied the correction function to the samples measured isotope ratios. The final $\delta^{34}S$ is presented as the average $\delta^{34}S$ of *n*-spots relative to Vienna Canyon Diablo Troilite (eqn (1)), while the uncertainties are expressed as one sigma (1σ) standard deviation.

3. Results and discussion

3.1 IRMS assigned sulfur isotopic composition of the samples

3.1.1 The pyrite samples. The IRMS $\delta^{34}S$ value of −1.19 ± 0.15‰ (V-CDT, $n = 5$) from Ward's pyrite is in good agreement with the reported value (−1.00 ± 0.2‰).[22] The mean $\delta^{34}S$ for the Huanzala pyrite micro-drilled spots is 1.93 ± 0.82‰ (V-CDT, $n = 14$), but the sulfur isotope values vary from −0.64 to +3.07‰ across the crystal facet with distinguishable zonation pattern. The zonation-related $\delta^{34}S$ variability of the Huanzala pyrite limits its use as an in-house reference material. Thus, we only used this pyrite in the subsequent experiments to tune the LA-ICP-MS/MS instrument. Given that Balmat pyrite pieces were in limited quantities, we used them to verify the accuracy of our *in situ* S isotope measurements by analysing them alongside other samples. Therefore, we favoured Ward's pyrite as in-house reference materials to correct for the instrumental mass bias during the subsequent pyrite LA-ICP-MS/MS measurements.

Additionally, the micro-drilled $\delta^{34}S$ values for the Zf-pyrite are −11.1‰ and −9.87‰ ($n = 2$). The studied Zf-pyrite's $\delta^{34}S$ composition is within range of [−20 to 0] ‰ of the $\delta^{34}S$ values obtained from metamorphosed strata at the contacts of mafic magmatic intrusions with sedimentary host rocks of the FAR-DEEP 12AB core, located ∼3 km to the north of the Maksovo quarry.[36]

3.1.2 Pyrrhotite samples. Uljaste pyrrhotite samples varied from −1.40‰ to −6.01‰ ($n = 2$ for each sample). The working value for the Ward's pyrrhotite standard was the same operating value in paragraph 2.1.

3.2 The effect of signal-smoothing devices

For all configurations, the measurement uncertainty and reproducibility based on uncorrected isotope ratios of nine spot analyses are presented in Table 3.

Table 3 Summary of the interface configuration performance data for S reaction product analysis

Interface configuration	Reproducibility RSD in ‰ ($n = 9$)	Measurement uncertainty ($\pm 1\sigma$, $n = 9$) in ‰	Washout A/B	Washout A/C
Configuration A for SO	4.3	1.8	68.1	70.8
Configuration A for SO_2	9.1	2.1	22.7	22.9
Configuration B for SO	2.9	1.7	64.0	66.1
Configuration B for SO_2	2.4	2.0	22.5	22.7
Configuration C for SO	2.0	1.7	50.7	58.0
Configuration C for SO_2	3.2	2.2	20.5	21.9
Configuration D for SO	1.9	1.7	48.9	58.8
Configuration D for SO_2	1.8	1.8	20.5	22.0

Adding coils to the TPE tubing and the cyclonic spray chamber improves the stability of the signal, resulting in better reproducibility and measurement uncertainty between the spot analyses. With maximal smoothing (configuration D), reproducibility for SO^+ is reduced from 4.3 to 1.9‰ and from 9.1 to 1.8‰ for SO_2^+, compared to the minimal smoothing in configuration A. In this study, the primary function of the cyclonic spray chamber is to act as a mixing chamber, homogenizing the aerosol before it enters the plasma. The coiled tubing serves a specific function: it is used to remove larger particles from the laser aerosol flow through centrifugal force. These larger particles can contribute to significant elemental and isotopic fractionation in the plasma due to incomplete ionization.[26] However, compared to SO^+, the SO_2^+ signal to background ratio as indicated by Washout A/C is lower affecting the observed measurement uncertainty.

In Fig. 3, the representative washout profiles are shown. For experimental configurations A and B, the washout between intervals A/B and A/C is comparable, and the baseline signal is achieved 10 seconds after the ablation ends. By looking at Fig. 3, in the 62–63 s range, it can be seen that the TPE tubing coiling in C configuration introduces a slight delay in signal drop. Adding the cyclonic spray chamber in configurations C and D further increases the washout times and background signal, as seen by the difference between A/B and A/C interval values compared to configurations A and C (Fig. 3 and Table 3). An increase in the background signal for configurations C and D could arise from the connections between the added cyclonic spray chamber and air permeation through the connections. Although the washout time was increased, background equivalent signals were achieved 20 s after the end of ablation. To reduce possible sample carryover effects, regular cleaning of the sample introduction system using high flows of inert gas or air is conducted.

For subsequent measurements of sulfur isotope ratios of the unknown samples and standard materials, we increased the number of coils to seven on the TPE tubing, which was the maximum number attainable with the tubing length used in the experiments. We noticed that seven coils lowered the measurement uncertainty of configuration D to 0.7‰ (Table 4).

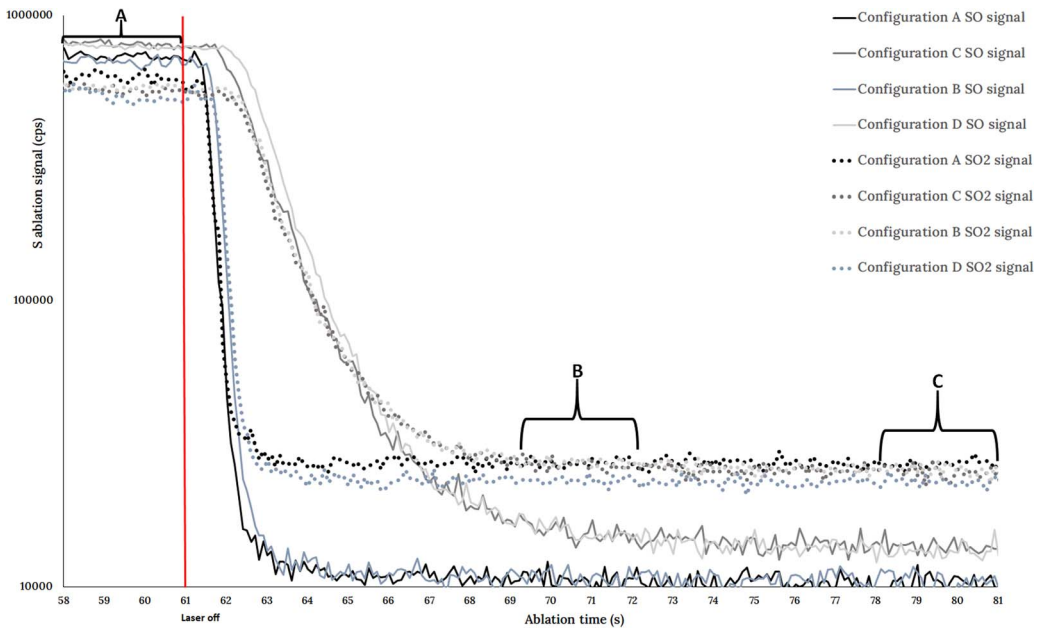

Fig. 3 Signal tailings after applying signal-smoothing configurations. Only one representative signal is shown in the picture.

Table 4 Seven times coiled TPE tubing + squid + cyclonic spray chamber configuration on different detection mode experiments

Analysis mode on configuration D with 7 coils	Reproducibility RSD in ‰ ($n = 9$)	Measurement uncertainty ($\pm 1\sigma$, $n = 9$) in ‰	Washout A/B	Washout A/C
Pulse–pulse spots	2.2	1.9	17.4	18.2
Pulse-analog lines	5.5	4.8	27.8	29.0
Pulse-analog spots	3.6	0.9	16.7	17.2
Natural pyrrhotite sample experiment	2.0	0.7	19.3	19.7

3.3 The effects of N_2O and N_2O + He on sulfur signal

The effect of N_2O as a reaction gas on the SO^+ and SO_2^+ reaction product signal intensities were tested over a range of N_2O gas flows (from 10 to 100% 4th cell gas flow) while laser ablation parameters remained constant:

The main interferences arising from the use of N_2O as reaction gas on the SO^+ reaction product are N_2O^+ and possibly O_3^+ ions and for SO_2^+ reaction products the O_4^+ ion cluster ($O_2^+ \cdot O_2$).[37]

The N_2O was selected as a reaction gas owing to its enhanced reaction efficiency towards sulfur, when compared to more commonly used O_2 gas.[38]

The $^{32}S^{16}O^+$ signal intensity was the highest at 20% N_2O (~300 000 cps), and from 15% N_2O, the $^{32}S^{16}O_2$ signal intensity surpassed that of $^{32}S^{16}O^+$ and reached peak intensity (~550 000 cps) at 35% N_2O (Fig. 4). Although highest SO_2^+ product ions signal was achieved at 35% N_2O flow rate, the background signal at $m/z = 64$ increases with N_2O flow rate. This trend is likely due to the enhanced formation of the O_4^+ ion cluster ($O_2^+ \cdot O_2$)[37] caused by higher N_2O gas density in the collision-reaction cell. As the disassociation energy required for breaking the NN–O bond is 1.7 eV, with increased N_2O flow the O_2 availability increases and follows the reaction principle as eqn (4):[38]

$$O_2^+ + 2O_2 \leftrightharpoons O_4^+ + O_2 \quad (4)$$

Increase in the O_4^+ ion formation during this ion–gas reaction pathway have been shown to increase with increasing gas density in the reaction chamber in SIFT instruments.[39]

Based on signal smoothing experiments, it was, however, evident that the signal-to-background ratio for the $^{32}S^{16}O_2^+$ reaction product was approximately 3 times lower than that of the $^{32}S^{16}O^+$ reaction product under comparable conditions, expressed as the A/C ratio in Table 3. The reason behind this difference could be due to a higher formation rate of $^{16}O_4^+$ ions compared to $^{14}N_2{}^{18}O^+$ ions under the tested conditions. Therefore, we tested how the addition of He to the collison reaction cell at different N_2O gas flows would influence the reaction efficiency of $^{32}S^{16}O^+$ and $^{32}S^{16}O_2^+$ product ion production.

The investigation's purpose was to see if using an inert gas in addition to a reactive gas changes could change the reaction dynamics to affect the product ion distribution and formation rate. In our case, He was used as a collision gas.

The combination of N_2O and He as cell gases significantly attenuates the $^{32}S^{16}O_2$ signal, reducing detector counts to below 200 000 cps across all N_2O and He flow rate configurations (Fig. 5). In contrast, the $^{32}S^{16}O$ signal amplifies considerably, and the optimal He flow rate depends on the N_2O flow rate. The optimal conditions for $^{32}S^{16}O^+$ product ion generation are achieved when using a mixture of a 5% N_2O flow rate and a He flow rate of 4.5 mL min^{-1}. Notably, for SO^+ product ions at a 20% N_2O flow rate with a He flow rate of less than 3 mL min^{-1}, the combination of reactive and inert gases yields superior results relative to the use of pure N_2O. The $^{32}S^{16}O$ signal intensity is approximately 350 000 cps (Fig. 5), compared to about 300 000 cps when using N_2O alone at the optimum 20% concentration (Fig. 4). Under the optimized analytical conditions for SO^+ and SO_2^+ ion formation, the background signal at

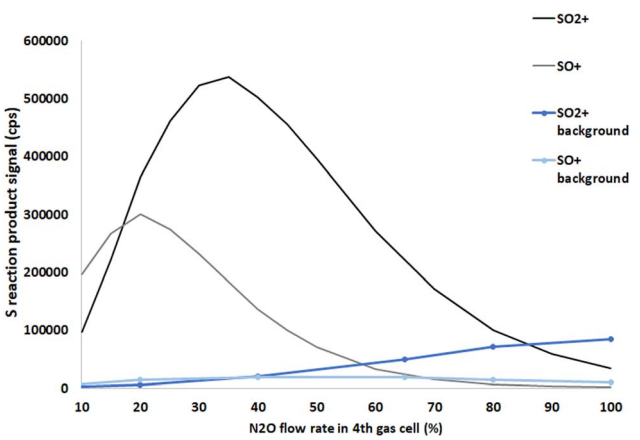

Fig. 4 The reaction efficiency and background signals under different flow rates of N_2O gas as signal intensities of $^{32}S^{16}O$ and $^{32}S^{16}O_2$ product ions.

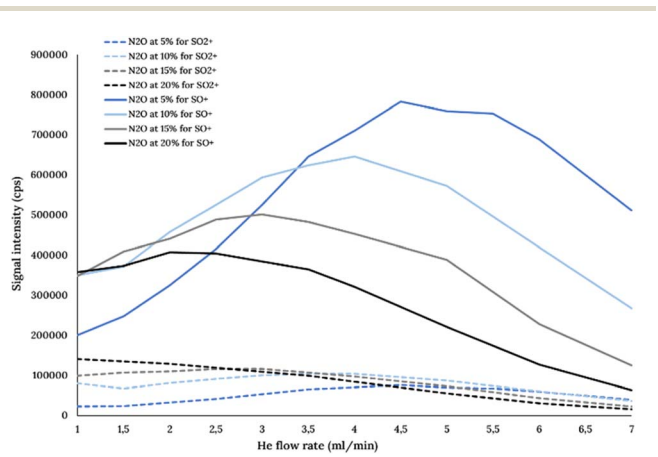

Fig. 5 The reaction efficiency under different He and N_2O gas flow rates as signal intensities of $^{32}S^{16}O$ and $^{32}S^{16}O^2$ product ions.

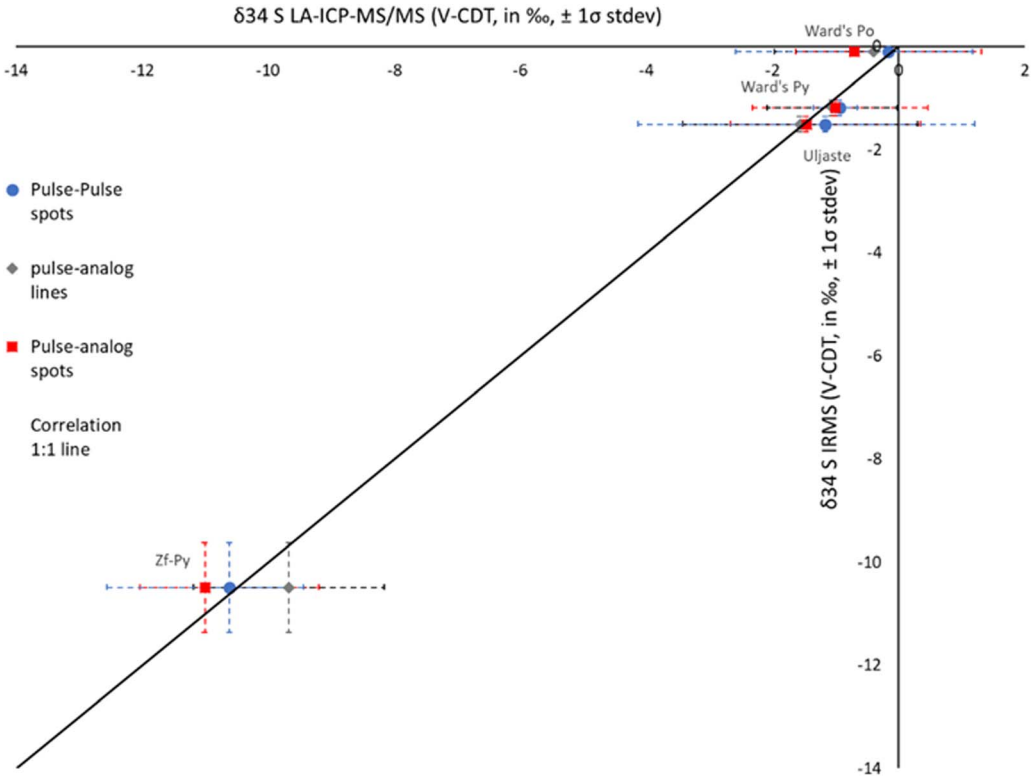

Fig. 6 Sulfur isotope ratios of pyrite and pyrrhotite samples in different detection modes normalized by Ward's pyrite.

$m/z = 64$ (for SO_2^+) was 2 times higher than at $m/z = 48$ (for SO^+). Owing to the higher signal intensity, $^{32}S^{16}O$-based signals exhibited approximately 3 times higher signal-to-background ratio than their $^{32}S^{16}O_2$-based counterparts when other analytical conditions were identical.

3.4 Effect of detection mode and sample matrix on $\delta^{34}S$ measurements

We selected two in-house reference materials- Ward's pyrite and pyrrhotite-as reference materials to correct for the instrumental mass bias during measurement of sulfur isotopic ratios in our natural sulfide samples. In addition, we investigated measuring the sulfur signals in different detection modes. These modes included maintaining the $^{32}S^{16}O^+$ and $^{34}S^{16}O_2^+$ reaction product signal in pulse detection mode during spot analysis and then changing analysis conditions so that the $^{32}S^{16}O$ signal would be collected in analog mode for spot and line ablations. The measured sulfur isotope ratios were normalized using Wards pyrite (Fig. 6) and pyrrhotite (Fig. 7) in-house reference materials and compared to the values obtained by IRMS analysis. For samples with single IRMS analysis result, error of 0.2‰ was used in Fig. 6–8. When multiple analysis results were available, experimentally determined 1σ values were applied.

For Zf-pyrite, a slight negative bias is observed in pulse–pulse mode when normalized with pyrite (−0.12‰). In contrast, pulse-analog mode for line scans shows positive bias (0.82‰), which becomes even more pronounced when using pyrrhotite as the reference material (2.73‰). Additionally, in pulse-analog mode spot analysis, the bias is inconsistent—positive when normalized with pyrite and negative when normalized with pyrrhotite.

For Uljaste pyrrhotite sample a positive bias was observed in case of both normalization procedures (Fig. 6 and 7). It was noticed that the variabilities obtained for the Zf-pyrite and Uljaste samples are within the uncertainty range of the IRMS control value when normalizing with either pyrrhotite or pyrite reference materials.

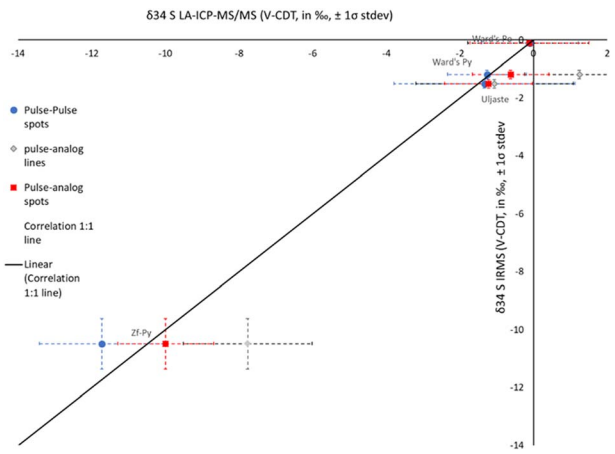

Fig. 7 Sulfur isotope ratios of pyrite and pyrrhotite samples in different detection modes normalized by Ward's pyrrhotite.

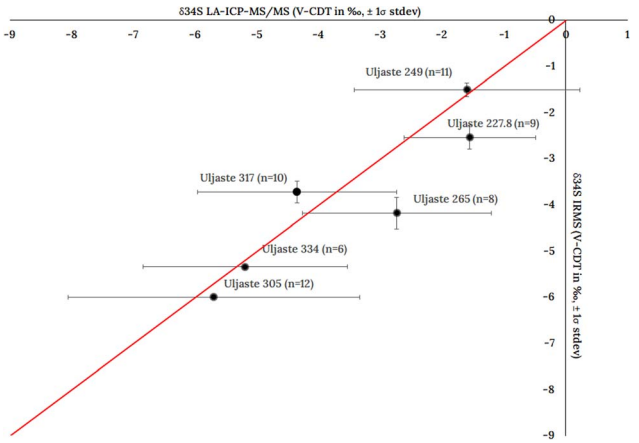

Fig. 8 Comparison of the LA-ICP-MS with the IRMS control values for Uljaste pyrrhotite samples. Number of analysis (*n*) is for LA-ICP-MS/MS dataset.

The results show that Ward's pyrite sample exhibits a smaller bias (−0.07‰) in pulse–pulse mode when normalized with pyrrhotite. However, considering the standard deviation values, normalization with Ward's pyrite provides better precision (standard deviation of 0.35‰, compared to 1.07‰ with Ward's pyrrhotite).

Conversely, the Ward's pyrrhotite sample aligns well with IRMS values across all detection modes when normalized with pyrrhotite. In contrast, the best precision is achieved in pulse–pulse mode under this normalization (standard deviation 1σ = 1.32‰ compared to 1.65‰ in pulse-analog lines and 1.62‰ in pulse-analog spots). When normalized with Wards pyrite the 1σ deviations were between 1.45 to 1.88‰ and a larger bias was observed. However, in pulse–pulse mode the bias was minimal (−0.05‰)

In the subsequent experiments, we used the pulse–pulse mode for analysis. The pyrite samples were normalized using Ward's pyrite, while pyrrhotite samples were normalized with Ward's pyrrhotite.

3.5 Measurements of the natural pyrite and pyrrhotite samples

The sulfur isotope ratios δ^{34}S of pyrite and pyrrhotite samples were derived by applying the methodologies outlined for signal smoothing, reaction gas combinations, and detector modes. We present the δ^{34}S values from multiple spot analyses within the same textural regions of individual pyrite and pyrrhotite samples, along with their associated uncertainties calculated as 1σ standard deviation. The isotope ratios for the Uljaste pyrrhotite samples are illustrated in Fig. 8, and for the Balmat and Zf-pyrite are presented in Table 5.

The Uljaste 249, Uljaste 334 and Uljaste 305 samples generally follow the 1 : 1 correlation line, suggesting that the δ^{34}S values obtained from LA-ICP-MS/MS and IRMS are consistent. On the other hand, Uljaste 227.8 and Uljaste 265 samples exhibit positive bias (0.98‰ and 1.45‰, respectively), while Uljaste 317 has a negative bias (−0.62‰). Even though, generally, the measured average δ^{34}S values for the pyrrhotite samples fall within 1 to 1.5‰ of the IRMS obtained control values, the variability is higher compared to the IRMS results. This variability could be due to the variation of the δ^{34}S in natural pyrrhotite samples. As the drill core diameter used to drill and collect the sample material subjected to IRMS is 10 times larger than the laser beam diameter used to ablate the pyrrhotite samples, larger variations in results would be expected for LA-ICP-MS/MS analysis. Initially 12 ablation spots were marked on each sample. The final number of spots used in calculations in some of the samples was reduced because the laser drifted from the original location, resulting in ablations falling on cracked surfaces or surrounding matrix thus being excluded (Fig. S4 in ESI†).

The Balmat pyrite shows a good agreement with the reported values with a slight positive bias and a relatively low standard deviation compared to the Zf-pyrite. Lowest observed standard deviation (0.35‰) was observed for isotopically homogenous Ward's pyrite when using Ward's pyrrhotite for normalisation. The standard deviation achieved on Wards pyrrhotite when normalised using Ward's pyrite was 1.32‰. Accuracy, expressed as bias, was below 0.3‰ for all 4 samples (Table 5).

The difference in precision of the results between the Balmat and Zf-pyrite could be due to the sample homogeneity. Balmat is a widely characterized sample with consistent results in its applications. On the other hand, the Zf-pyrite is a more heterogeneous natural pyrite sample, and the significant variability could be attributed to the inhomogeneous distribution of the S isotope ratios. On the other hand, the two reference materials Ward's pyrite and pyrrhotite differ slightly from their IRMS values with a low standard deviation.

Table 5 Sulfur isotope ratios expressed as δ^{34}S, 1σ standard deviation and bias values in ‰ for samples. All the samples are normalized with Ward's pyrite, and samples denoted with * are normalized using Ward's pyrrhotite. Data collected in pulse–pulse mode

Sulfide samples	LA-ICP-MS/MS value	1σ standard deviation	IRMS	1σ standard deviation	Bias
ZF pyrite ($n = 7$)	−10.29	1.70	−10.49	0.87	0.21
Balmat pyrite ($n = 9$)	15.40	0.98	15.10	0.20	0.29
Ward's pyrite ($n = 10$)	−0.96	0.35	−1.19	0.15	0.23
Ward's pyrite * ($n = 10$)	−1.26	1.07	−1.19	0.15	0.05
Ward's pyrrhotite ($n = 10$)	−0.16	1.88	−0.11	0.5	0.05
Ward's pyrrhotite* ($n = 10$)	−0.10	1.32	−0.11	0.5	0.01

4. Conclusions

This study presents a novel method for characterizing sulfur isotope ratios in sulfide minerals, focusing on pyrite and pyrrhotite, using LA-ICP-MS/MS. Our approach advances *in situ* $\delta^{34}S$ determinations using quadrupole-based ICP-MS systems, which face limitations due to polyatomic interferences at $m/z = 32$ and $m/z = 34$ and low sulfur sensitivity. When using pure N_2O as reaction gas at a flow rate of 35% of the 4th cell gas flow rate, the highest sensitivity was achieved for the SO_2^+ reaction product. Adding a He flow to the reaction cell alongside N_2O, the primary reaction product shifted from SO_2^+ to SO^+. The optimal gas flow rate to achieve the highest product ion signal intensity was 5% flow rate on the 4th cell gas using N_2O and 4.5 mL per min He. By using a mixture of N_2O and He in the collision cell while keeping other analytical parameters constant, an increase of 1.4 times in the primary production signal relative to using only N_2O can be achieved. Owing to the higher signal intensity, $^{32}S^{16}O$-based signals exhibited approximately 3 times higher signal-to-background ratio than their $^{32}S^{16}O_2$-based counterparts when other analytical conditions were identical.

Through the combined use of a "squid", a coiled TPE tubing and a cyclonic spray chamber, the highest signal smoothing effects were achieved as observed by the lowest measurement uncertainty. The signal smoothing compartments such as coiled TPE tubing and the cyclonic spray chamber mitigate the issue of large particles being produced using a Nd: YAG laser. Although increasing the number of signal smoothing components increased the washout time, background equivalent signals were achieved 20 s after the end of ablation.

By comparing the results of natural pyrite and pyrrhotite samples normalized using Wards pyrite and pyrrhotite in-house reference materials, matrix dependent bias was observed. The bias was smaller than the measurement uncertainty of the analysis, but for the analysis of the unknown samples, the use of matrix matched reference material is preferred. To minimize the effects of the isotopic fractionation arising from different sources, the sample-standard bracketing approach with ablation of the matrix matched standards under the same analytical conditions was applied.

Under optimized analytical conditions with signal collection in pulse mode detection only, good alignment with IRMS control values for natural samples was achieved. For Uljaste pyrrhotite samples, our measurement values were within ±1.5‰ of IRMS values, with a 1σ standard deviation of 1.1–2.4‰. For isotopically homogenous sulfide samples, the 1σ standard deviation was in the range of 0.35–1.88‰ and the method uncertainty can conservatively be assumed to be in the range of 1–1.5‰. Conversely, accuracy for the isotopically homogenous samples was within ±0.3‰ of reference values.

This study provides a promising approach for characterizing sulfur isotopic ratio variability in natural samples using LA-ICP-MS/MS. Although there are limitations in precision as compared to the LA-MC-ICP-MS technique, this method can be applied to identify samples with sufficiently variable sulfur isotope ratios. Most promisingly, for samples where microbial induced isotopic fractionation, with $\delta^{34}S$ ranging from [−50 to 0] ‰, can be expected. Owing to the lower instrument capital costs, the developed method can also be considered as a more available or affordable pre-screening tool, prior to more detailed $\delta^{34}S$ investigations.

Data availability

The data supporting this article have been included as part of the ESI.†

Author contributions

E. Eensoo: conceptualization, data curation, formal analysis, investigation, methodology, writing – original draft, writing – review & editing. P. Paiste: conceptualization, data curation, formal analysis, funding acquisition, investigation, methodology, project administration, supervision, writing – review & editing. K. Paiste: conceptualization, funding acquisition, project administration, supervision, writing – review & editing. D. Fike: resources, writing – review & editing. J. Houghton: resources, writing – review & editing.

Conflicts of interest

There are no conflicts to declare.

Acknowledgements

This project has received funding from the European Union's Horizon 2020 research and innovation programme under the Marie Sklodowska-Curie grant agreement No. 894831. We thank J. Valley for sharing pieces of the Balmat pyrite.

Notes and references

1 D. Rickard and G. W. Luther, Chemistry of iron sulfides, *Chem. Rev.*, 2007, **107**(2), 514–562, DOI: **10.1021/cr0503658**.
2 R. O. Rye and H. Ohmoto, Sulfur and carbon isotopes and ore genesis: a review, *Econ. Geol.*, 1974, **69**(6), 826–842, DOI: **10.2113/gsecongeo.69.6.826**.
3 R. R. Large, V. V. Maslennikov, F. Robert, L. V. Danyushevsky and Z. Chang, Multistage sedimentary and metamorphic origin of pyrite and gold in the giant sukhoi log deposit, Lena Gold province, Russia, *Econ. Geol.*, 2007, **102**(7), 1233–1267, DOI: **10.2113/gsecongeo.102.7.1233**.
4 H. V. Thomas, R. R. Large, S. W. Bull, V. Maslennikov, R. F. Berry, R. Fraser, S. Froud and R. Moye, Pyrite and pyrrhotite textures and composition in sediments, laminated quartz veins, and reefs at bendigo gold mine, Australia: insights for ore genesis, *Econ. Geol.*, 2011, **106**(1), 1–31, DOI: **10.2113/econgeo.106.1.1**.
5 A. Amrani, Organosulfur compounds: molecular and isotopic evolution from biota to oil and gas, *Annu. Rev. Earth Planet. Sci.*, 2014, **43**(42), 733–768, DOI: **10.1146/annurev-earth-050212-124126**.

6 C. Cai, H. Li, K. Li and D. Wang, Thermochemical sulfate reduction in sedimentary basins and beyond: a review, *Chem. Geol.*, 2022, **607**, 121018, DOI: 10.1016/j.chemgeo.2022.121018.
7 H. Ohmoto, T. Kakegawa and D. R. Lowe, 3.4-billion-year-old biogenic pyrites from barberton, South Africa: sulfur isotope evidence, *Science*, 1993, **262**(5133), 555–557, DOI: 10.1126/science.11539502.
8 D. T. Johnston, J. Farquhar, K. S. Habicht and D. E. Canfield, Sulphur Isotopes and the search for life: strategies for identifying sulphur metabolisms in the rock record and beyond, *Geobiology*, 2008, **6**(5), 425–435, DOI: 10.1111/j.1472-4669.2008.00171.x.
9 D. A. Fike, A. S. Bradley and C. V. Rose, Rethinking the ancient sulfur cycle, *Annu. Rev. Earth Planet. Sci.*, 2015, **43**(1), 593–622, DOI: 10.1146/annurev-earth-060313-054802.
10 H. Cui, K. Kitajima, M. J. Spicuzza, J. H. Fournelle, A. Denny, A. Ishida, F. Zhang and J. W. Valley, Questioning the biogenicity of neoproterozoic superheavy pyrite by SIMS, *Am. Mineral.*, 2018, **103**(9), 1362–1400, DOI: 10.2138/am-2018-6489.
11 V. Pasquier, R. N. Bryant, D. A. Fike and I. Halevy, Strong local, not global, controls on marine pyrite sulfur isotopes, *Sci. Adv.*, 2021, **7**(9), eabb7403, DOI: 10.1126/sciadv.abb7403.
12 H. G. Machel, Bacterial and thermochemical sulfate reduction in diagenetic settings — old and new insights, *Sediment. Geol.*, 2001, **140**(1–2), 143–175, DOI: 10.1016/S0037-0738(00)00176-7.
13 A. Lecomte, M. Cathelineau, R. Michels, C. Peiffert and M. Brouand, Uranium mineralization in the alum shale formation (Sweden): evolution of a U-rich marine black shale from sedimentation to metamorphism, *Ore Geol. Rev.*, 2017, **88**, 71–98, DOI: 10.1016/j.oregeorev.2017.04.021.
14 K. Paiste, D. A. Fike, K. Kirsimäe, C. Jones and A. Lepland, Testing the global significance of the sulfur isotope record of the ca. 2.0 Ga zaonega formation: a micro-scale S isotope investigation, *Geochim. Cosmochim. Acta*, 2022, **331**, 86–104, DOI: 10.1016/j.gca.2022.05.021.
15 J. R. Craig, The metamorphism of pyrite and pyritic ores: an overview, *Mineral. Mag.*, 1993, **57**(386), 3–18, DOI: 10.1180/minmag.1993.057.386.02.
16 A. J. Hall, A. J. Boyce and A. E. Fallick, Iron sulphide sulfides in metasediments: isotopic support for a retrogressive pyrrhotite to pyrite reaction, *Chem. Geol. Isot. Geosci. Sect.*, 1987, **65**(3–4), 305–310, DOI: 10.1016/0168-9622(87)90010-8.
17 N. H. S. Oliver, T. C. Hoering, T. W. Johnson, D. Rumble and W. C. Shanks, Sulfur isotopic disequilibrium and fluid-rock interaction during metamorphism of sulfidic black shales from the waterville-augusta Area, Maine, USA, *Geochim. Cosmochim. Acta*, 1992, **56**(12), 4257–4265, DOI: 10.1016/0016-7037(92)90266-L.
18 T. Wagner and A. J. Boyce, Pyrite metamorphism in the devonian hunsruck slate of Germany: insights from laser microprobe sulfur isotope analysis and thermodynamic modeling, *Am. J. Sci.*, 2006, **306**(7), 525–552, DOI: 10.2475/07.2006.02.
19 D. E. Canfield, R. Raiswell, J. T. Westrich, C. M. Reaves and R. A. Berner, The use of chromium reduction in the analysis of reduced inorganic sulfur in sediments and shales, *Chem. Geol.*, 1986, **54**(1–2), 149–155, DOI: 10.1016/0009-2541(86)90078-1.
20 D. E. Crowe and R. G. Vaughan, Characterization and use of isotopically homogeneous standards for *in situ* laser microprobe analysis of $^{34}S/^{32}S$ ratios, *Am. Mineral.*, 1996, **81**(1–2), 187–193, DOI: 10.2138/am-1996-1-223.
21 M. Chaussidon, F. Albarède and S. M. F. Sheppard, Sulphur isotope variations in the mantle from ion microprobe analyses of micro-sulphide sulfide inclusions, *Earth Planet. Sci. Lett.*, 1989, **92**(2), 144–156, DOI: 10.1016/0012-821X(89)90042-3.
22 R. N. Bryant, C. Jones, M. R. Raven, M. L. Gomes, W. M. Berelson, A. S. Bradley and D. A. Fike, Sulfur isotope analysis of microcrystalline iron sulfides using secondary ion mass spectrometry imaging: extracting local paleo-environmental information from modern and ancient sediments, *Rapid Commun. Mass Spectrom.*, 2019, **33**(5), 491–502, DOI: 10.1002/rcm.8375.
23 C. Jones, D. A. Fike and K. M. Meyer, Secondary ion mass spectrometry methodology for isotopic ratio measurement of micro-grains in thin sections: true grain size estimation and deconvolution of inter-grain size gradients and intra-grain radial gradients, *Geostand. Geoanalytical Res.*, 2019, **43**(1), 61–76, DOI: 10.1111/ggr.12247.
24 L. R. Riciputi, B. A. Paterson and R. L. Ripperdan, Measurement of light stable isotope ratios by SIMS, *Int. J. Mass Spectrom.*, 1998, **178**(1–2), 81–112, DOI: 10.1016/S1387-3806(98)14088-5.
25 P. R. Craddock, O. J. Rouxel, L. A. Ball and W. Bach, Sulfur isotope measurement of sulfate and sulfide by high-resolution MC-ICP-MS, *Chem. Geol.*, 2008, **253**(3–4), 102–113, DOI: 10.1016/j.chemgeo.2008.04.017.
26 S. E. Gilbert, L. V. Danyushevsky, T. Rodemann, N. Shimizu, A. Gurenko, S. Meffre, H. Thomas, R. R. Large and D. Death, Optimisation of laser parameters for the analysis of sulphur isotopes in sulphidesulfide minerals by laser ablation ICP-MS, *J. Anal. Spectrom.*, 2014, **29**(6), 1042–1051, DOI: 10.1039/C4JA00011K.
27 O. Peter, F. Melcher and C. Walkner, *In situ measurement of sulfur isotopic composition ($\delta^{34}S$) in sphalerite using LA-(QQQ)-ICP-MS*, 2017.
28 P. R. D. Mason, J. Košler, J. C. M. De Hoog, P. J. Sylvester and S. Meffan-Main, *In situ* determination of sulfur isotopes in sulfur-rich materials by laser ablation multiple-collector inductively coupled plasma mass spectrometry (LA-MC-ICP-MS), *J. Anal. Spectrom.*, 2006, **21**(2), 177–186, DOI: 10.1039/B510883G.
29 F. Börner, M. Keith, J. L. Bücker, P. Voudouris, R. Klemd, K. Haase, M. Kutzschbach and F. Schiperski, *In situ* trace element and S isotope systematics in pyrite from three porphyry-epithermal prospects, limnos island, Greece, *Front. Earth Sci.*, 2022, **10**, 916107, DOI: 10.3389/feart.2022.916107.

30 D. E. Crowe, J. W. Valley and K. L. Baker, Micro-analysis of sulfur-isotope ratios and zonation by laser microprobe, *Geochim. Cosmochim. Acta*, 1990, **54**(7), 2075–2092, DOI: **10.1016/0016-7037(90)90272-M**.

31 M. J. Whitehouse, B. S. Kamber, C. M. Fedo and A. Lepland, Integrated Pb- and S-isotope investigation of sulphidesulfide minerals from the early archaean of Southwest Greenland, *Chem. Geol.*, 2005, **222**(1–2), 112–131, DOI: **10.1016/j.chemgeo.2005.06.004**.

32 R. Kozdon, N. T. Kita, J. M. Huberty, J. H. Fournelle, C. A. Johnson and J. W. Valley, *In situ* sulfur isotope analysis of sulfide minerals by SIMS: precision and accuracy, with application to thermometry of ~3.5 Ga pilbara cherts, *Chem. Geol.*, 2010, **275**(3–4), 243–253, DOI: **10.1016/j.chemgeo.2010.05.015**.

33 G. Skrzypek, C. E. Allison, J. K. Böhlke, L. Bontempo, P. Brewer, F. Camin, J. F. Carter, M. M. G. Chartrand, T. B. Coplen, M. Gröning, J.-F. Hélie, G. Esquivel-Hernández, R. A. Kraft, D. A. Magdas, J. L. Mann, J. Meija, H. A. J. Meijer, H. Moossen, N. Ogrinc, M. Perini, A. Possolo, K. M. Rogers, A. Schimmelmann, A. Shemesh, D. X. Soto, F. Thomas, R. Wielgosz, M. R. Winchester, Z. Yan and P. J. H. Dunn, Minimum requirements for publishing hydrogen, carbon, nitrogen, oxygen and sulfur stable-isotope delta results (IUPAC technical report), *Pure Appl. Chem.*, 2022, **94**(11–12), 1249–1255, DOI: **10.1515/pac-2021-1108**.

34 C. E. Rees, Sulphur isotope measurements using SO_2 and SF_6, *Geochim. Cosmochim. Acta*, 1978, **42**(4), 383–389, DOI: **10.1016/0016-7037(78)90269-7**.

35 Z.-Y. Zhu, S.-Y. Jiang, C. L. Ciobanu, T. Yang and N. J. Cook, Sulfur isotope fractionation in pyrite during laser ablation: implications for laser ablation multiple collector inductively coupled plasma mass spectrometry mapping, *Chem. Geol.*, 2017, **450**, 223–234.

36 K. Paiste, A. Pellerin, A. L. Zerkle, K. Kirsimäe, A. R. Prave, A. E. Romashkin and A. Lepland, The pyrite multiple sulfur isotope record of the 1.98 Ga zaonega formation: evidence for biogeochemical sulfur cycling in a semi-restricted basin, *Earth Planet. Sci. Lett.*, 2020, **534**, 116092.

37 J.-H. Yang and D. C. Conway, Bonding in ion clusters. I. O_4^+, *J. Chem. Phys.*, 1964, **40**(6), 1729–1735.

38 S. T. Lancaster, T. Prohaska and J. Irrgeher, Characterisation of gas cell reactions for 70+ elements using N_2O for ICP tandem mass spectrometry measurements, *J. Anal. At. Spectrom.*, 2023, **38**(5), 1135–1145, DOI: **10.1039/D3JA00025G**.

39 A. B. Raksit, Reactions of O_2^+, O_4^+ and $O_2^+ \cdot H_2O$ ions with neutral molecules, *Int. J. Mass Spectrom. Ion Process.*, 1986, **69**(1), 45–65, DOI: **10.1016/0168-1176(86)87041-0**.